



OPEN ACCESS

EDITED BY

Georgios Bikas,
Georg Simon Ohm University of Applied
Sciences Nuremberg, Germany

REVIEWED BY

Jinlong Liu,
Zhejiang University, China
Giancarlo Sorrentino,
Istituto di Scienze e Tecnologie per l'Energia e
la Mobilità Sostenibili (STEMS) - CNR, Italy

*CORRESPONDENCE

Epaminondas Mastorakos,
✉ em257@eng.cam.ac.uk

RECEIVED 19 September 2024

ACCEPTED 12 December 2024

PUBLISHED 30 January 2025

CITATION

Kylikas A and Mastorakos E (2025) Simulations of decane-ammonia autoignition in two mixture fractions.
Front. Mech. Eng. 10:1498820.
doi: 10.3389/fmech.2024.1498820

COPYRIGHT

© 2025 Kylikas and Mastorakos. This is an open-access article distributed under the terms of the [Creative Commons Attribution License \(CC BY\)](https://creativecommons.org/licenses/by/4.0/). The use, distribution or reproduction in other forums is permitted, provided the original author(s) and the copyright owner(s) are credited and that the original publication in this journal is cited, in accordance with accepted academic practice. No use, distribution or reproduction is permitted which does not comply with these terms.

Simulations of decane-ammonia autoignition in two mixture fractions

Angelos Kylikas¹ and Epaminondas Mastorakos^{1,2*}

¹Department of Engineering, University of Cambridge, Cambridge, United Kingdom, ²Cambridge Centre for Advanced Research and Education in Singapore (CARES), Singapore, Singapore

This paper presents a zero-dimensional Doubly Conditional Moment Closure (0D-DCMC) methodology for investigating dual-fuel combustion involving ammonia and diesel. The approach uses two mixture fractions as conditioning variables, one for each fuel, to effectively model ignition and reveal the flame structure in mixture fraction space. Initially, 0D reactor calculations are performed using Cantera, exploring the chemical mechanism, identifying the most reactive mixture fractions, and determining key species involved in the ignition process. Following that, the 0D-DCMC simulations carried out provide understanding into the effects of the scalar and cross-scalar dissipation rates on autoignition. The results show that higher scalar dissipation rates delay ignition, while a negative cross-scalar dissipation rate reduces ignition delay compared to a positive rate. The ignition is shown to occur near the most reactive mixture fraction of the most reactive fuel, at lower conditional values of the less reactive fuel's mixture fraction. The species fronts formed are observed to follow a trajectory between the stoichiometric mixture fractions of the fuels. The results establish a robust computational framework for modeling dual-fuel combustion.

KEYWORDS

ammonia, conditional moment closure, non-premixed, decane, dual-fuel

1 Introduction

Following the Paris Agreement in 2015 (UNFCCC, 2024), the International Maritime Organisation is aiming at 50% greenhouse gas emissions reduction compared to 2008 by 2050 (Joung et al., 2020). Shipping is responsible for carrying around 80% of global trade by volume (United Nations, 2018) producing however an estimated 2.2% of global emissions CO₂ (International Maritime Organization, 2015). With increasing environmental regulations and mounting concerns about greenhouse gas emissions (Simon et al., 2020), the search for cleaner alternative fuels has become imperative (Chin et al., 2021). Ammonia has emerged as a promising candidate due to its carbon-free nature (Ramanathan et al., 2023) and the potential to significantly reduce marine pollution (Wong et al., 2024). Due to its zero carbon and sulfur content, burning NH₃ in an engine results in almost no CO₂ or SO_x emissions with potential for reducing GHG by 94% (Zhou et al., 2024). From a well-to-wake standpoint, ammonia is a carbon-neutral fuel when it is generated using renewable energy sources (MAN Energy Solutions, 2023). The elimination of pollutants also includes soot, unburned hydrocarbons, methane slip, and CO.

However, ammonia is a difficult fuel to burn. The flame speed is low and its ignition time long (Valera-Medina et al., 2018), which necessitates special measures to consume it successfully. One such approach is dual-fuel combustion and in particular pilot ignition,

where an easy-to-ignite hydrocarbon fuel is injected into the cylinder first, so that its ignition provides a distributed ignition source for the ammonia. Reciprocating engines are expected to be one the key technologies for using ammonia in shipping in the future (Curran et al., 2024). If the ammonia is already premixed with air, then an ammonia premixed flame will initiate, but if the ammonia is injected separately as in a direct injection concept, there will be a non-premixed ammonia-air system that must be ignited. This paper deals with the latter possibility and provides some fundamental understanding of the underlying chemistry and how this is affected by diffusion.

Revealing the fundamental effects of simultaneous mixing and chemical reaction is often done by resort to the mixture fraction, as in the flamelet method [for a review, see the textbooks (Poinso and Veynante, 2005; Peters, 2001)]. In our dual-fuel case, however, we need two mixture fractions. In the current analysis, the Doubly Conditional Moment Closure method presented by Sitte and Mastorakos (Philip, 2019) is extended to a two-mixture fraction approach. There have been previous efforts in 2D flamelet calculations using the two mixture fraction approach in staged combustion (secondary oxidizer stream) (Perry et al., 2017; Yu and Watanabe, 2023) accurately capturing the flame structure of the combustion system, but there have not been explorations of flame structures in mixture fraction space for hydrocarbon-ammonia systems. Here, the general features of hydrocarbon ignition will be mimicked by decane, for which detailed chemistry is available.

The objectives of this paper are to study decane-ammonia combustion systems, and in particular decane autoignition and the subsequent ignition of the ammonia-air flame, through a Doubly-Conditional Moment Closure formulation. The structure of the flames is explored and the sensitivity to scalar dissipation quantified.

2 Numerical methods

2.1 Flamelet and CMC

In the standard flamelet approach, the functions $T(\xi, t)$, $Y_k(\xi, t)$ define the flame structure if we assume that the structure of the diffusion flame depends only on the mixture fraction ξ and on time t . This is substantiated by making a variable change in the species equations from (x_1, x_2, x_3, t) to (z, y_2, y_3, t) where y_2 and y_3 are spatial variables in planes parallel to iso- ξ surfaces (Poinso and Veynante, 2005).

$$T = T(\xi, t) \text{ and } Y_k = Y_k(\xi, t) \quad (1)$$

Neglecting the terms associated with gradients along the flame front (y_2 and y_3) and keeping the terms perpendicular to the flame (along ξ) as significant we could approximate the flame structure locally as one-dimensional, depending only on time and the coordinate normal to the flame front (ξ) as presented in Equation 1. For this assumption to hold the flame must be thin compared to other flow and wrinkling scales in a multi-dimensional flow (Poinso and Veynante, 2005). This implies that each part of the flame front can be approximated as a small laminar flame, the “flamelet”.

Following the above the species mass fraction equation as well as the temperature are written as follows in Equations 2, 3:

$$\rho \frac{\partial Y_k}{\partial t} = \dot{\omega}_k + \frac{1}{2} \rho \chi \frac{\partial^2 Y_k}{\partial \xi^2} \quad (2)$$

$$\rho \frac{\partial T}{\partial t} = \dot{\omega}_T + \frac{1}{2} \rho \chi \frac{\partial^2 T}{\partial \xi^2} \quad (3)$$

The only term depending on spatial variables (x_i), in the flamelet Equations 2, 3 is the scalar dissipation rate χ which controls mixing as it dictates the gradients of ξ (Poinso and Veynante, 2005). Once χ is specified, Equations 2, 3 can be solved in the ξ space to provide the flame structure. The usual way to determine its value/distribution is by performing a direct numerical simulation of the problem under consideration or an experiment. If this is not the case, a try error process is followed in order to allocate what is called the extinction scalar dissipation rate over which the flame cannot exist.

The flamelet equations can also be understood as a subset of the Conditional Moment Closure approach, reviewed in Bilger (1993), where the conditioning is performed based on the mixture fraction (Peters, 2001). Rather than focusing on flame surface statistics and the laminar reactive-diffusive structure tied to the flame surface as is the case in the flamelet model, CMC employs conditional moments at a particular location x and time t within the flow field, using the conditional probability density function (Peters, 2001). The flame structure is characterized by the conditional averages of the reactive scalars and the conditional mean Q_α is defined as the ensemble average of $Y_\alpha(x, t)$ under the condition that the associated value $\xi(x, t)$ is at the value η (Philip, 2019) as seen in Equation 4:

$$Q_\alpha(\eta; x, t) \equiv \langle Y_\alpha(x, t) | \xi(x, t) = \eta \rangle \equiv \langle Y_\alpha | \eta \rangle \quad (4)$$

Through this averaging process, the instantaneous reactive scalar value can be recovered into the conditional mean and a deviation from the conditional mean as presented in Equation 5 (Bilger, 1993):

$$Y_\alpha(x, t) = Q_\alpha(\xi(x, t); x, t) + Y''_\alpha(x, t) \quad (5)$$

The core concept of the CMC method involves solving transport equations for the conditional averages of reactive scalars in order to determine the flame structure (Philip, 2019). Furthermore, an exact transport equation for these conditional moments can be derived. That is by adopting a set of assumptions, including high Reynolds number, the primary closure hypothesis, molecular-level Fickian mass diffusion, a Lewis number of unity, and negligible conditional density fluctuations, the equation can be simplified to the form of Equation 6 (Klimenko and Bilger, 1999):

$$\frac{\partial Q_\alpha}{\partial t} + \langle u | \eta \rangle \cdot \nabla Q_\alpha = \langle N_\xi | \eta \rangle \frac{\partial^2 Q_\alpha}{\partial \eta^2} + \langle \dot{\omega}_\alpha | \eta \rangle - \frac{\nabla \cdot (\langle \rho | \eta \rangle \langle u'' Y''_\alpha | \eta \rangle p(\eta))}{\langle \rho | \eta \rangle p(\eta)} \quad (6)$$

The unconditional mean of a variable can be determined from its conditional means as follows:

$$\langle Y_\alpha(x, t) \rangle = \int_0^1 Q_\alpha(\eta; x, t) p(\eta; x, t) d\eta \quad (7)$$

2.2 DCMC equations

The DCMC equations presented in this sub-section are adapted from the work of Philip (2019). The rationale for using double conditioning is that if most fluctuations around the single-conditional mean can be linked to the second conditional variable, then the fluctuations around the double-conditional mean, determined by two mixture fractions, should be small (Philip, 2019). As singly-conditioned CMC models are limited to cases that are either premixed or predominantly non-premixed (Philip Sitte and Mastorakos, 2019) the double conditioning allows for a wider description of phenomena present in dual fuel systems. The DCMC method extends the parameter space and incorporates the cross-scalar dissipation rate, while remaining a straightforward generalization of the CMC approach. Additionally, it is expected to describe well all combustion modes relevant to dual-fuel engines (Harikrishnan et al., 2024). The doubly conditional space is as follows in Equation 8:

$$D = \{(\eta_1, \eta_2) \in \mathbb{R}^2 : 0 \leq \eta_1 \leq 1, 0 \leq \eta_2 \leq 1\} \quad (8)$$

The conditional mass fractions are given in Equation 9 and the conditional enthalpy in Equation 10. The conditional temperature equation also exists but only one of the temperature and enthalpy need to be solved choosing the latter:

$$\begin{aligned} \frac{\partial Q_\alpha}{\partial t} + \nabla \cdot (Q_\alpha \langle \mathbf{u} | \eta_1, \eta_2 \rangle) &= Q_\alpha \nabla \cdot (\langle \mathbf{u} | \eta_1, \eta_2 \rangle) \\ &- \frac{1}{\bar{\rho} \bar{p}} \nabla \cdot (\bar{\rho} \bar{p} [\langle \mathbf{u} Y_\alpha | \eta_1, \eta_2 \rangle - Q_\alpha \langle \mathbf{u} | \eta_1, \eta_2 \rangle]) \\ &+ \frac{1}{\bar{\rho} \bar{p}} \nabla \cdot (\bar{\rho} \bar{p} \langle D \nabla Y_\alpha | \eta_1, \eta_2 \rangle) \\ &+ \langle N_{\xi_1} | \eta_1, \eta_2 \rangle \frac{\partial^2 Q_\alpha}{\partial \eta_1^2} + 2 \langle N_{\xi_1 \xi_2} | \eta_1, \eta_2 \rangle \frac{\partial^2 Q_\alpha}{\partial \eta_1 \partial \eta_2} \\ &+ \langle N_{\xi_2} | \eta_1, \eta_2 \rangle \frac{\partial^2 Q_\alpha}{\partial \eta_2^2} + \langle \dot{\omega}_\alpha | \eta_1, \eta_2 \rangle \\ &- \langle \dot{\omega}_c^* | \eta_1, \eta_2 \rangle \frac{\partial Q_\alpha}{\partial \eta_2} \end{aligned} \quad (9)$$

$$\begin{aligned} \frac{\partial Q_h}{\partial t} + \nabla \cdot (Q_h \langle \mathbf{u} | \eta_1, \eta_2 \rangle) &= Q_h \nabla \cdot (\langle \mathbf{u} | \eta_1, \eta_2 \rangle) \\ &- \frac{1}{\bar{\rho} \bar{p}} \nabla \cdot (\bar{\rho} \bar{p} [\langle u h | \eta_1, \eta_2 \rangle - Q_h \langle u | \eta_1, \eta_2 \rangle]) \\ &+ \frac{1}{\bar{\rho} \bar{p}} \nabla \cdot (\bar{\rho} \bar{p} \langle a \nabla h | \eta_1, \eta_2 \rangle) \\ &+ \langle N_{\xi_1} | \eta_1, \eta_2 \rangle \frac{\partial^2 Q_h}{\partial \eta_1^2} + 2 \langle N_{\xi_1 \xi_2} | \eta_1, \eta_2 \rangle \frac{\partial^2 Q_h}{\partial \eta_1 \partial \eta_2} \\ &+ \langle N_{\xi_2} | \eta_1, \eta_2 \rangle \frac{\partial^2 Q_h}{\partial \eta_2^2} \\ &- \langle \dot{\omega}_c^* | \eta_1, \eta_2 \rangle \frac{\partial Q_h}{\partial \eta_2} + \left\langle \frac{1}{\rho} \frac{\partial p}{\partial t} | \eta_1, \eta_2 \right\rangle \end{aligned} \quad (10)$$

where, according to Harikrishnan et al. (2024), the following are true: $\langle N_{\xi_1} | \eta_1, \eta_2 \rangle$, $\langle N_{\xi_2} | \eta_1, \eta_2 \rangle$, and $\langle N_{\xi_1 \xi_2} | \eta_1, \eta_2 \rangle$ are the conditional scalar dissipation rates (SDRs) of ξ_1 , ξ_2 , and the cross-scalar dissipation rate, respectively. The final term in the Q_h equation accounts for the pressure (p) rise in the constant volume chamber. The term $\langle \dot{\omega}_\alpha | \eta_1, \eta_2 \rangle$ represents the conditional chemical source term while the $\langle u | \eta_1, \eta_2 \rangle$, \bar{p} , and $\bar{\rho}$ are the conditional velocity, Favre-filtered probability density function, and filtered density,

respectively. Moving on, η_1 and η_2 are the respective sample space variables for the two mixture fractions. Finally, $\langle \dot{\omega}_c^* | \eta_1, \eta_2 \rangle$ is the conditional apparent reaction rate term. The apparent reaction rate, encapsulating both the direct chemical source term and effects of the effects of the scalar dissipation rates, is presented in Equation 11:

$$\begin{aligned} \langle \dot{\omega}_c^* | \eta_1, \eta_2 \rangle &= \frac{1}{\frac{\partial Q_\psi}{\partial \eta_2}} \left[\langle \dot{\omega}_\psi | \eta_1, \eta_2 \rangle + \langle N_{\xi_1} | \eta_1, \eta_2 \rangle \frac{\partial^2 Q_\psi}{\partial \eta_1^2} \right. \\ &\quad \left. + 2 \langle N_{\xi_1 \xi_2} | \eta_1, \eta_2 \rangle \frac{\partial^2 Q_\psi}{\partial \eta_1 \partial \eta_2} + \langle N_{\xi_2} | \eta_1, \eta_2 \rangle \frac{\partial^2 Q_\psi}{\partial \eta_2^2} \right] \end{aligned} \quad (11)$$

The conditional expectation of the mixture fraction SDR, $\langle N_\xi | \eta_1, \eta_2 \rangle$, presented in Equation 12 is modeled using Amplitude Mapping Closure (AMC) (O'Brien and Jiang, 1991) of Equation 13. The shape of this bell curve plays a significant role in the diffusion in mixture fraction space due to the zero value it assumes at the boundaries not allowing diffusion to those points from internal values of the mixture fraction.

$$\langle N_\xi | \eta_1, \eta_2 \rangle = N_0 G_\xi(\eta_1) \quad (12)$$

where,

$$G_\xi(\eta) = \exp(-2(\text{erf}^{-1}(2\eta - 1))^2) \quad (13)$$

$$N_0 = \frac{\tilde{N}_\xi}{\int_0^1 \int_0^1 G_\xi(\eta_1) \bar{p}(\eta_1, \eta_2) d\eta_1 d\eta_2} \quad (14)$$

$$N_{\xi_1} \equiv D \nabla \xi_1 \cdot \nabla \xi_1, \quad N_{\xi_2} \equiv D \nabla \xi_2 \cdot \nabla \xi_2, \quad N_{\xi_1 \xi_2} \equiv D \nabla \xi_1 \cdot \nabla \xi_2 \quad (15)$$

where $N_0 = \langle N_\xi | 0.5, \eta_2 \rangle$ and $\langle N_\xi | \eta_1, 0.5 \rangle$ respectively using Equation 14. The modeling of the cross-scalar dissipation rate is still a matter of research and constitutes a central input to the DCMC method. The modelling of the latter term of Equation 15 is proposed in Equation 16 by Kronenburg (2004) is utilized.

$$\langle N_{\xi_1 \xi_2} | \eta_1, \eta_2 \rangle = \frac{\sqrt{\tilde{N}_{\xi_1 \xi_2}}}{\sqrt{\tilde{N}_{\xi_1} \tilde{N}_{\xi_2}}} \sqrt{\langle N_{\xi_1} | \eta_1, \eta_2 \rangle} \sqrt{\langle N_{\xi_2} | \eta_1, \eta_2 \rangle} \quad (16)$$

The ratio $\frac{\sqrt{\tilde{N}_{\xi_1 \xi_2}}}{\sqrt{\tilde{N}_{\xi_1} \tilde{N}_{\xi_2}}}$ will be denoted by N_{rat} in this paper and its magnitude will be varied to examine the consequences to the solution. For partially premixed combustion, the cross-scalar dissipation rate is an important quantity and assumes a positive value for premixed combustion and a negative for non-premixed combustion (Chakraborty et al., 2007). There is very little information in the literature for this quantity whose modelling is a topic for further research.

2.3 0D-DCMC equations

To initially explore flame structures in dual-fuel systems, as in this paper, a simplification process is followed reducing the DCMC equations to zero dimension and essentially going from three spatial and two mixture fraction dimensions to only two mixture fraction dimensions. The underlying assumptions of the 0D-DCMC equations are.

- High Reynolds number that allows for the neglect of some molecular transport terms.
- Unity Lewis number meaning that all reacting scalars diffuse at the same rate with the mixture fraction.
- No transport in physical space, meaning that terms related to physical coordinates do not appear in the equations.
- No heat losses.
- Constant pressure.
- Fixed η boundaries and Dirichlet boundary conditions for $\eta = 0$ and $\eta = 1$.
- Presumed $N | \eta$ profiles.

Under these assumptions, the 0D-DCMC equations assume the form of Equations 17, 18.

$$\frac{\partial Q_\alpha}{\partial t} = \langle N_{\xi_1} | \eta_1, \eta_2 \rangle \frac{\partial^2 Q_\alpha}{\partial \eta_1^2} + 2 \langle N_{\xi_1 \xi_2} | \eta_1, \eta_2 \rangle \frac{\partial^2 Q_\alpha}{\partial \eta_1 \partial \eta_2} + \langle N_{\xi_2} | \eta_1, \eta_2 \rangle \frac{\partial^2 Q_\alpha}{\partial \eta_2^2} + \langle \dot{\omega}_\alpha | \eta_1, \eta_2 \rangle \quad (17)$$

$$\frac{\partial Q_h}{\partial t} = \langle N_{\xi_1} | \eta_1, \eta_2 \rangle \frac{\partial^2 Q_h}{\partial \eta_1^2} + 2 \langle N_{\xi_1 \xi_2} | \eta_1, \eta_2 \rangle \frac{\partial^2 Q_h}{\partial \eta_1 \partial \eta_2} + \langle N_{\xi_2} | \eta_1, \eta_2 \rangle \frac{\partial^2 Q_h}{\partial \eta_2^2} + \langle \dot{Q} | \eta_1, \eta_2 \rangle \quad (18)$$

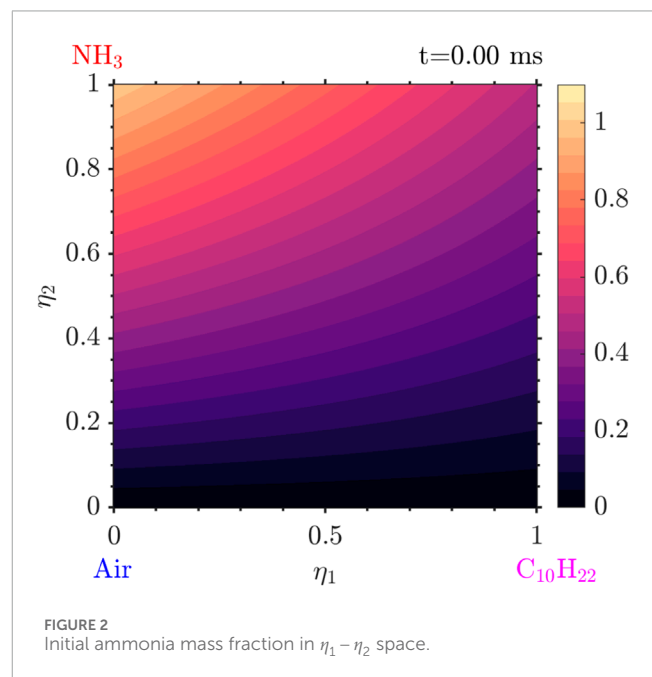
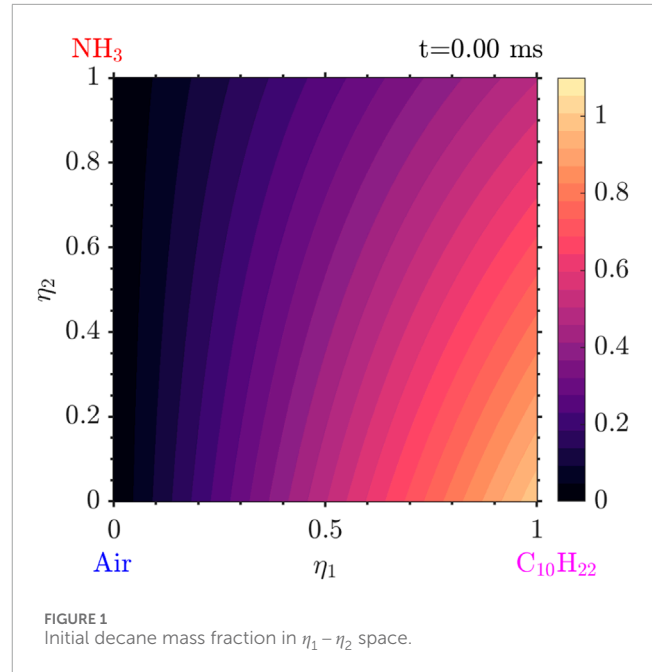
In this paper, 0D-DCMC simulations will be performed to understand the basic structure of dual-fuel autoignition systems, as a first step in a full implementation in a turbulent reacting flow multi-dimensional simulation.

2.4 Initial conditions

In this section, the initial conditions of the solution of the equations are discussed. Two mixture fractions are used, one for each fuel, ξ_1 for decane, and ξ_2 for ammonia. The initial conditions are chosen as mixing lines. These lines correspond to states where the fuel and oxidizer mix without reacting. Such mixing lines are crucial in capturing ignition and quenching (Poinso and Veynante, 2005).

With the presence of two fuels, it is not clear what to do in the top right corner. The points $(\eta_1, \eta_2) = (0, 1)$ and $(\eta_1, \eta_2) = (1, 0)$ correspond to pure ammonia and pure diesel respectively whereas the point $(\eta_1, \eta_2) = (0, 0)$ to the pure oxidizer (air). The point $(\eta_1, \eta_2) = (1, 1)$ is a matter of debate as there are multiple options and it is unclear whether this results in different results. As we have two fuels the logical boundary condition is to consider that at that point 50% ammonia and 50% diesel (by mass) are present corresponding to a mixture. The resulting distributions are seen in Figures 1, 2. One could also set this point as 100% ammonia or diesel altering the mathematical formulation of the problem and thus the results. However, the quantitative analysis yields the same conclusions. In conclusion, the current choice is a matter of modelling and is not expected to affect the results if the interpretation is done correctly considering the initial conditions.

As the chemistry is detailed and the c_p of each species is different, the initial distributions of species mass fractions and the enthalpy are linear functions of ξ_1 and ξ_2 . However, the temperature is not. In the current analysis, the mass fractions and the enthalpy are used and the temperature distribution is computed from the enthalpy.



The same typical approach as in the single mixture fraction case is followed for constructing the mixing lines in each of the four boundaries interpolating between the extreme values at the two corners corresponding to each boundary. The values at the inner nodes are computed from a multivariate interpolation.

2.5 Numerical procedure

The 0D-DCMC equation is a parabolic PDE in two dimensions (the two mixture fractions) and time. In a full 3D simulation in the future, we would add the 3 spatial dimensions, as in Philip,

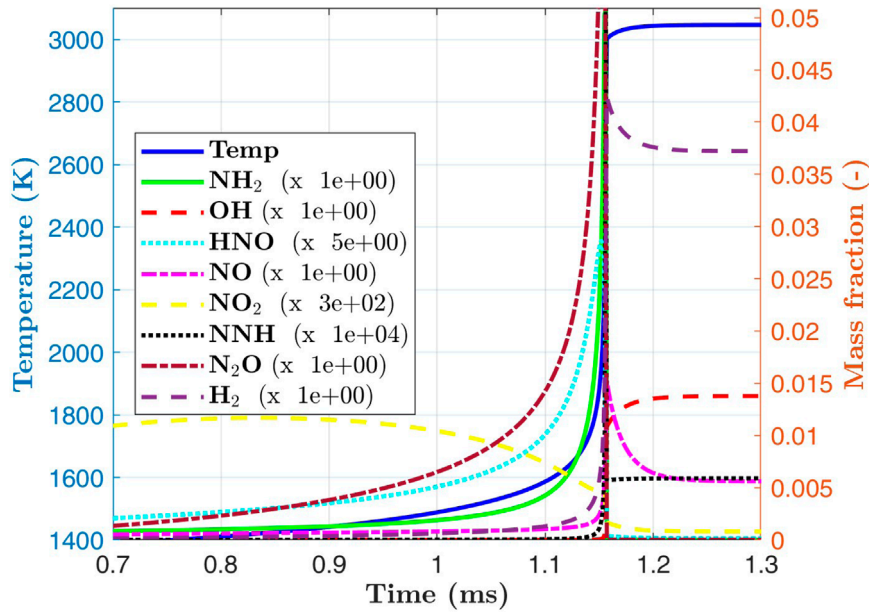


FIGURE 3 Temperature and various species during autoignition of ammonia/air for $T_{air} = 1200$ K, $P = 20$ bar, $\phi = 1$.

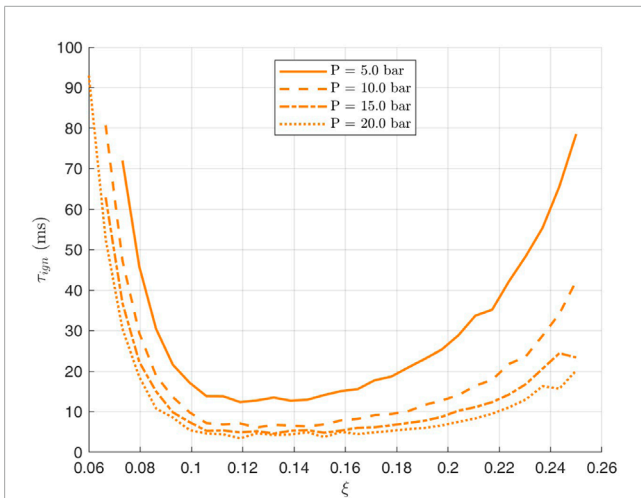


FIGURE 4 Variation of ammonia ignition delay with mixture fraction ξ for different pressures for $T_{ox} = 1200$ K and $T_f = 300$ K.

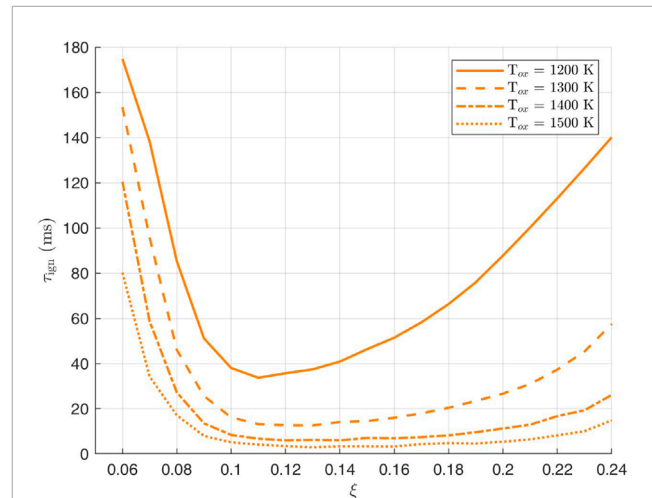
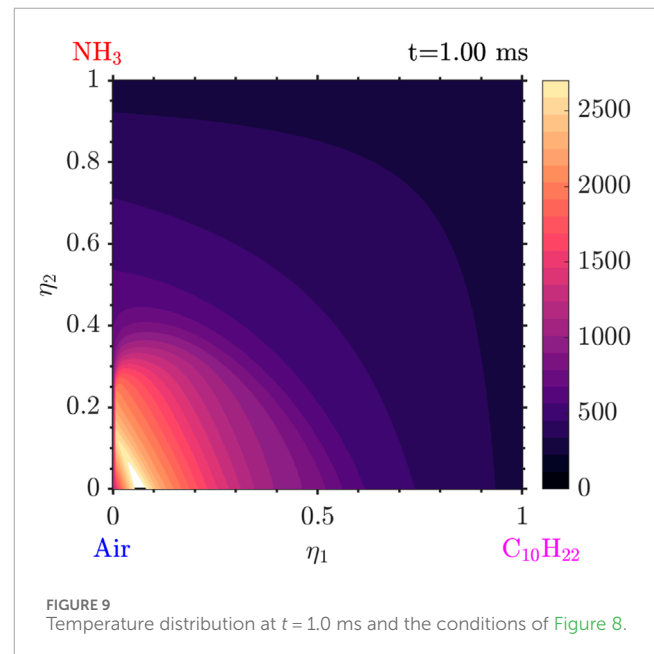
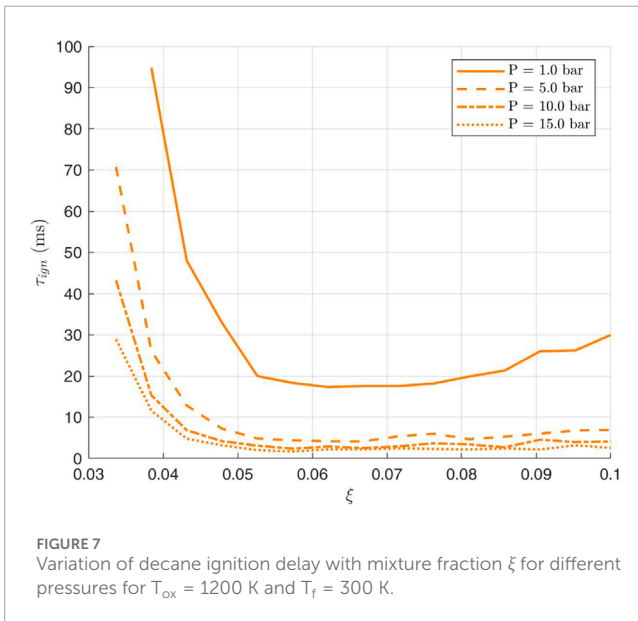
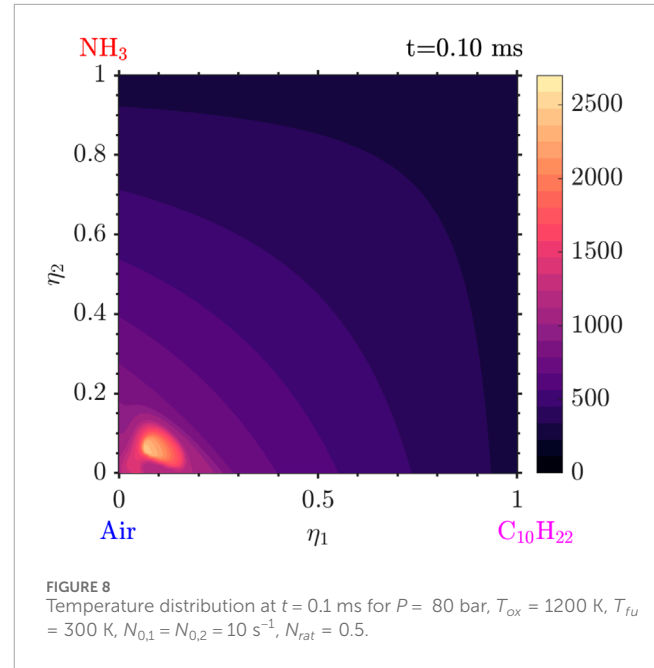
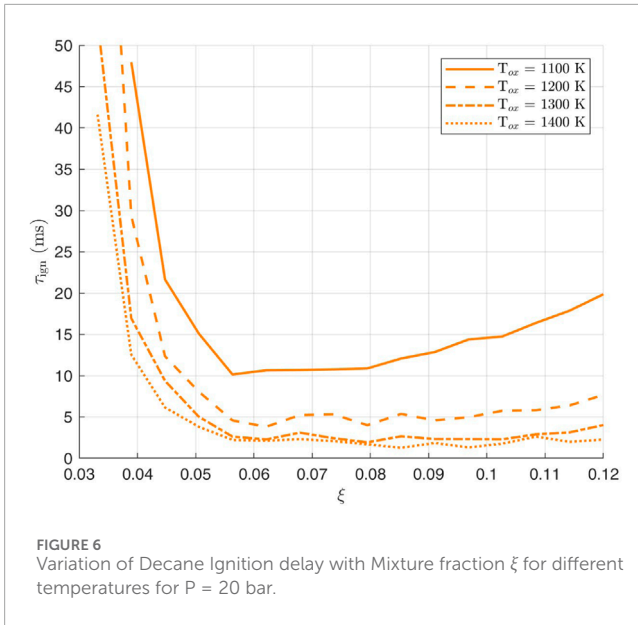


FIGURE 5 Variation of ammonia ignition delay with mixture fraction ξ for different temperatures for $P = 20$ bar and $T_f = 300$ K.

(2019), but this is not done here. The mixture fraction spaces are discretised with a 71 x 71 nonuniform grid covering the whole range of 0–1. The choice of its size is dictated by the trade-off between accuracy and computational effort. The grid is denser around the stoichiometric mixture fraction of each fuel as the flame and most reactions are expected to lie there. Due to the steep gradients and the rapid construction and destruction of species around stoichiometry, a very dense grid is required around there for accuracy. As a result, using a non-uniform grid allows for significant computational improvements. The diffusion in mixture

fraction space is solved first with the VODPK solver (Alan, 1983), using the non-stiff Adam’s method which solves the set of non-linear ODEs. Central-differencing schemes for non-uniform grids, which are second-order accurate, are used for the numerical discretisation of the $\frac{\partial^2 Q}{\partial \xi^2}$ terms.

Chemical source terms are addressed last using the SpeedCHEM solver (Perini et al., 2012). This solver, referred to as LIBSC, utilizes a sparse Jacobian formulation and precomputed, temperature-dependent properties to greatly enhance computational speed. It also supports the use of an analytical



Jacobian, which approximates the Jacobian matrix of the ODE system. For most chemical mechanisms, this approach offers significant performance enhancements. Timesteps equal or smaller than 10^{-6} s are used to minimise operator splitting errors.

2.6 Chemical mechanism

This section briefly discusses the selection of the chemical mechanism used for the simulations. Typically, the physical properties of diesel, such as density and evaporation rate, are modeled using decane or dodecane, while heptane is used to mimic diesel's chemistry. Most current chemical mechanisms for

ammonia/hydrocarbon fuels are derived by merging databases for each fuel and as a result in general further research is required in this area.

A recently published chemical scheme, the Aalto75 model (Tolga Kurumus et al., 2024), includes 75 species and 451 reactions and is reported to be well-validated across various experimental datasets, including ignition delay times, laminar flame speeds, and species profiles. However, it was not used in this study as it was released after the project had already begun and is left for future work. Another chemical mechanism for ammonia/n-heptane mixtures was published by (Thorsen et al., 2023), offering

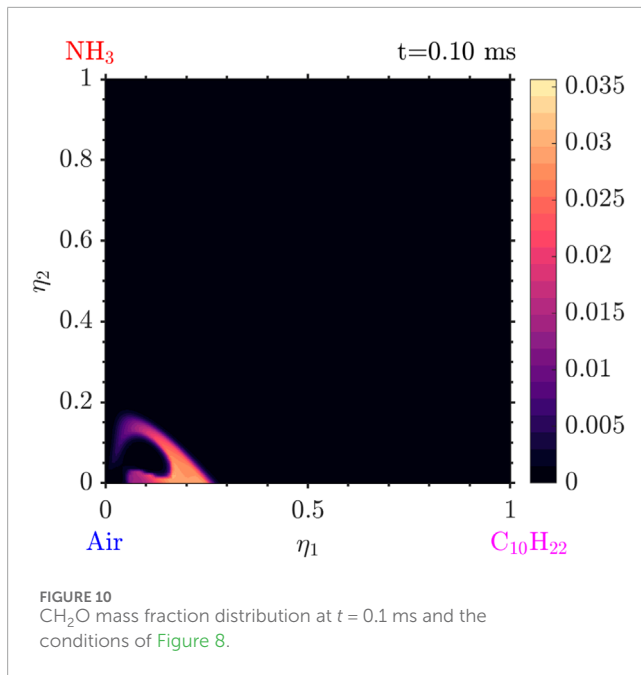


FIGURE 10
CH₂O mass fraction distribution at t = 0.1 ms and the conditions of Figure 8.

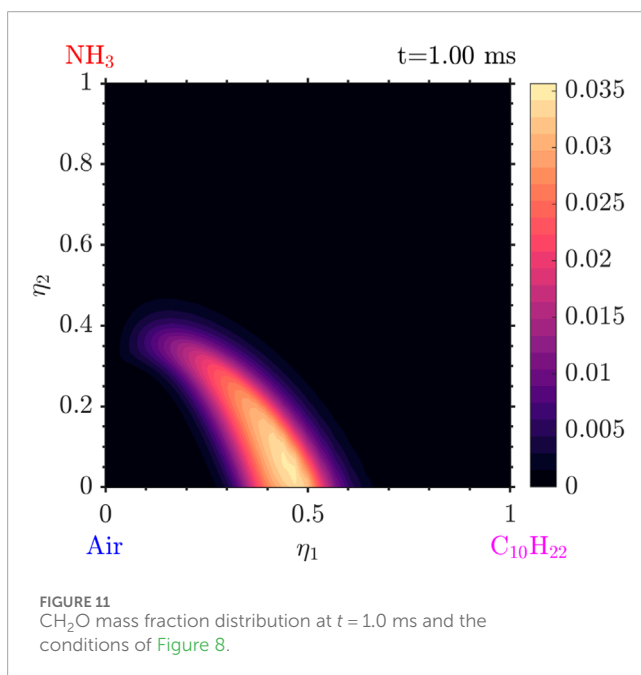


FIGURE 11
CH₂O mass fraction distribution at t = 1.0 ms and the conditions of Figure 8.

good predictions of ignition delay times at pressures up to 100 bar. However, this mechanism was not selected due to its complexity, as it has too many species and reactions, making it very difficult to handle computationally for the current project.

The chemical mechanism ultimately chosen for this study is the one provided by Lin Tay et al. (2017) for decane-ammonia combustion, consisting of 80 species and 374 reactions. The ignition delay times for diesel and ammonia were found to be very similar with the parent mechanisms, indicating that this mechanism is sufficiently robust for use in diesel engine simulations and should contain the key aspects of the problem.

3 Results and discussion

3.1 0D reactor evaluation

In this section, homogeneous reactor calculations with the use of Cantera are performed. The motivation is twofold: to validate that the chemical mechanism produces reasonable results for homogeneous mixtures and to locate the “most reactive” mixture fraction ξ_{mr} (Mastorakos, 2009) in the case of fuel-air mixing layers. For such cases, the initial condition of temperature is connected with the initial mass fractions through Equations 19–22:

$$Y_{fu} = \xi \times Y_{fu_0} \quad (19)$$

$$Y_{O_2} = (1 - \xi) \times Y_{O_{2_0}} \quad (20)$$

$$Y_{N_2} = (1 - \xi) \times Y_{N_{2_0}} \quad (21)$$

$$T = T_{ox} - \xi \times (T_{ox} - T_{fu}) \quad (22)$$

The temperature of the oxidizer is left as a parameter and the fuel temperature is set constant to 300 K. The calculations are based on a series of batch reactors for the different temperatures and pressures with the mixture fraction being varied with the initial condition as above. For each temperature or pressure, the most reactive mixture fraction is the one producing the smallest ignition delay.

A typical batch reactor simulation for the ignition of homogeneous ammonia/air mixtures is presented in Figure 3 for an oxidiser temperature of 1200 K and a pressure of 2 atm and it is found that ignition takes place at approximately 1.1 ms. We notice that the rapid temperature increase is correlated with the rise of the species OH and H₂ and that N₂O is rapidly produced and destroyed making it a pre-ignition species, as seen in the right axis of the mass fractions. N₂O, HNO, NO and NH₂ are quickly produced at the autoignition instant and then quickly destroyed. On the contrary, species like NNH and OH, although again rapidly produced, stay relatively constant after the ignition. Finally, observing the early chemistry we see that NO₂ is produced during the species accumulation period and flattens during the autoignition.

For the case of ammonia/air mixing layers, i.e., where the initial condition of species and temperature are the inert mixing between pure ammonia and pure air, Figures 4, 5 show the variation of ignition delay time with mixture fraction for different pressures and temperatures. These curves serve to locate the most reactive mixture fraction which is the minimum of those U-bell shapes. For low values of mixture fraction, despite the high temperatures, the mixture is too lean while for high mixture fractions, the temperature is low and the mixture too rich, and hence the minimum autoignition time is somewhere between and this characterises the most reactive mixture fraction. The most reactive mixture fraction ξ_{mr} for the given pressure of 20 bar and an oxidizer temperature of 1200 K is 0.11. For reference, the stoichiometric mixture fraction is $\xi_{st} = 0.142$. It is also evident that as the pressure or temperature increase, the most reactive mixture fraction determination becomes less sharp, which suggests that autoignition in non-premixed systems may be occurring almost simultaneously in wide regions in space (i.e., at a range of mixture fractions). Nevertheless, the estimate of ξ_{mr} and the associated

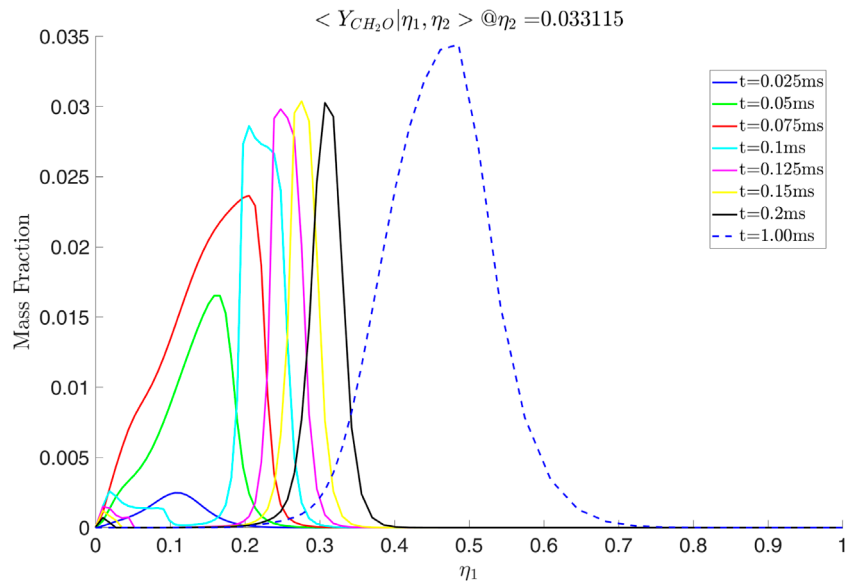


FIGURE 12
Conditional mass fraction of CH_2O at different instants for the conditions of Figure 8.

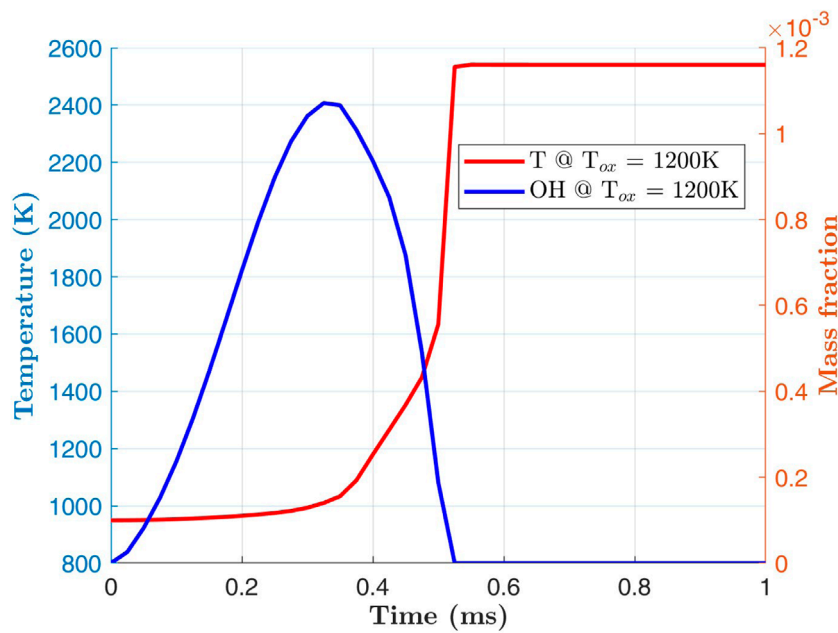
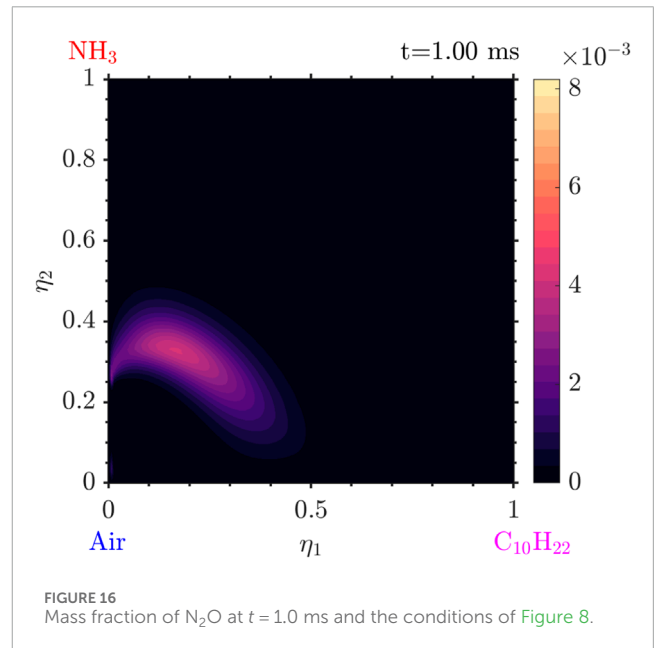
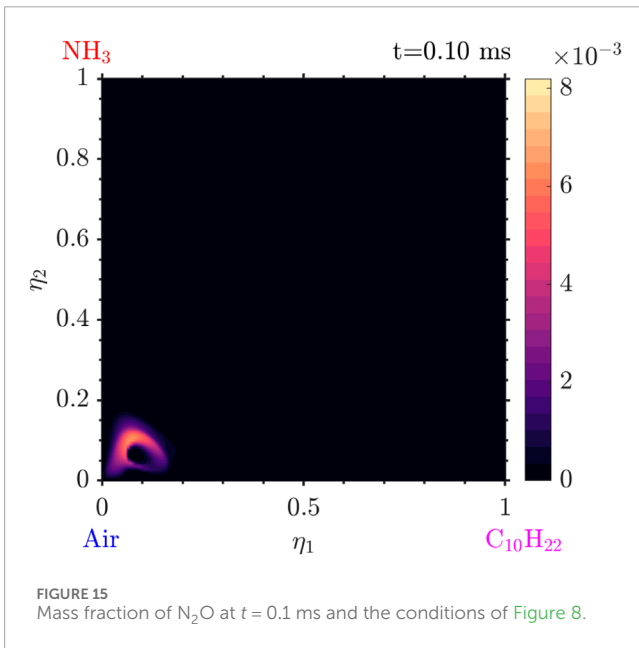
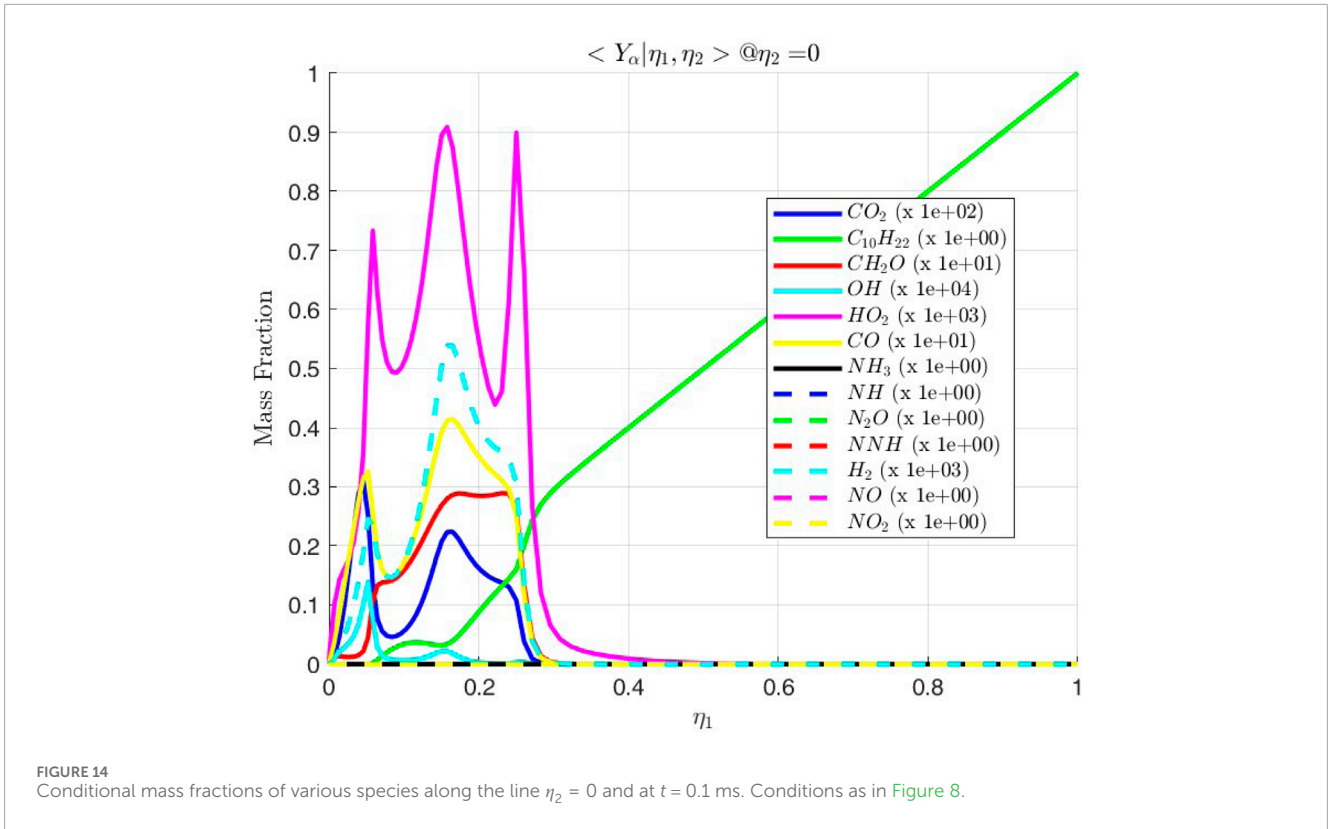


FIGURE 13
Time evolution of the temperature and the OH mass fraction at $(\eta_1, \eta_2) = (\xi_{1mr}, \xi_{2mr})$ and the conditions of Figure 8.

autoignition time are important reference values for inhomogeneous systems and can be compared when straining (e.g., through high values of the scalar dissipation) becomes important.

The same procedure is followed for the decane-air mixture. In Figures 6, 7 ignition delay in terms of the mixture fraction ξ_{mr} is presented for different pressures and temperatures. Again, similar trends are observed for lower values of ξ as expected from the stoichiometric $\xi_{st} = 0.0626$. Compared to ammonia,

decane ignites quickly for high temperatures and pressures. For example, for 20 bar and $T_{ox} = 1200$ K, the quickest ignition time for the ammonia-air system is about 35 ms, while for the decane-air system the quickest ignition delay is about 10 ms. Overall, the higher reactivity of decane is demonstrated in the chemical scheme used. Therefore, the concept that the high reactivity fuel (decane) will autoignite before the ammonia is captured well by the current mechanism.



3.2 Autoignition and evolution in 0D-DCMC

In this section, the 0D-DCMC exploration takes place to understand the effects of the scalar dissipation rates on the ignition of the decane-ammonia mixture. An overall description is given first, followed by a more detailed presentation of the structure of

the autoignition spot and the evolution of the reaction fronts. The sensitivity to scalar dissipation rates is also shown.

3.2.1 General behaviour

The results presented in this section are from a simulation for $T_{ox} = 1200$ K, $T_{fu} = 300$ K and a pressure of 80 bar. The peak scalar dissipation rate is set at 10 s^{-1} and a peak cross scalar dissipation rate

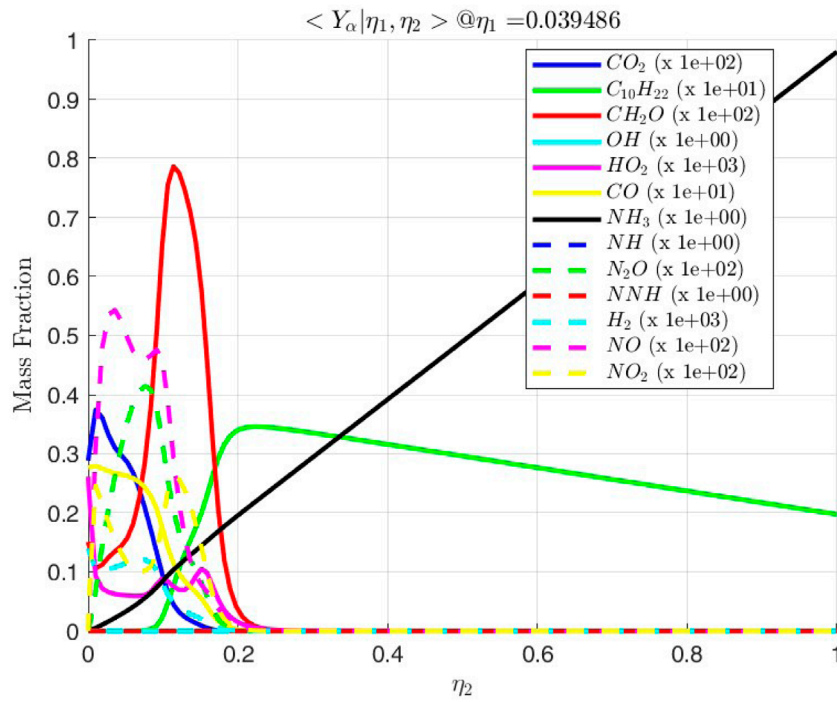


FIGURE 17 Conditional mass fractions as a function of η_2 at the indicated η_1 at $t = 0.1$ ms and the conditions of Figure 8.

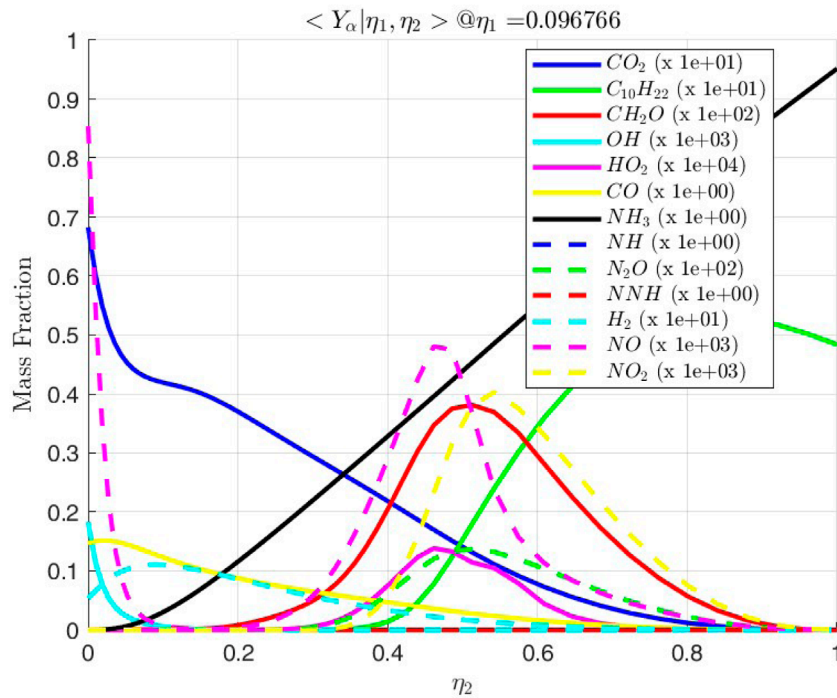
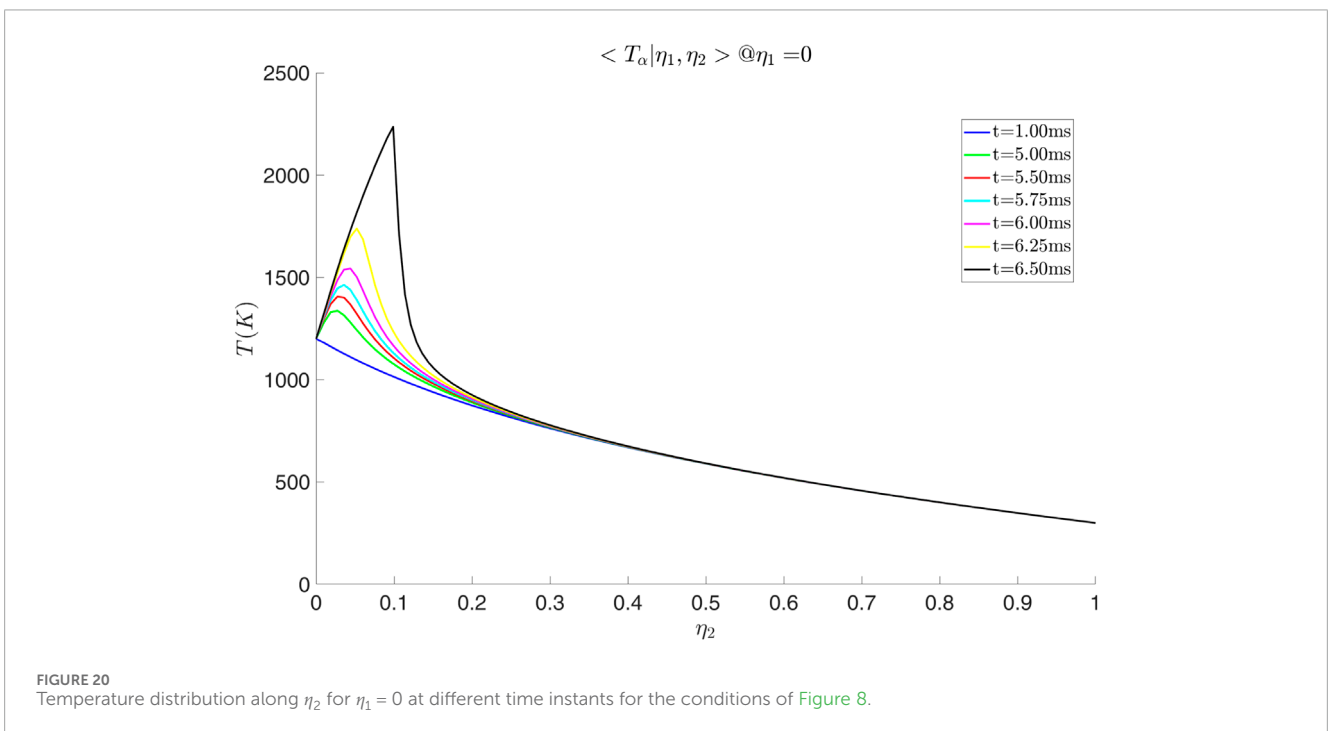
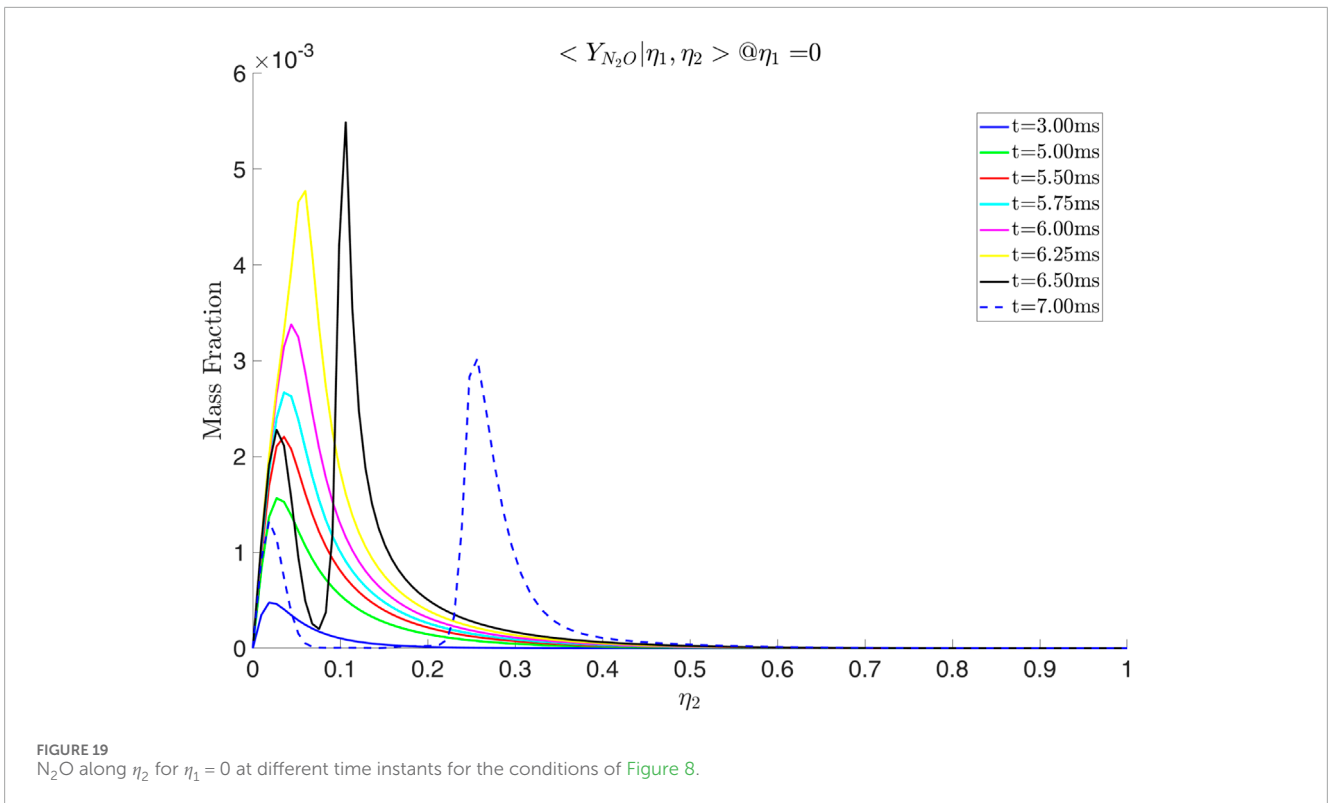


FIGURE 18 Conditional mass fractions vs. η_2 at the indicated η_1 at $t = 5.0$ ms and the conditions of Figure 8.



of -5 s^{-1} . A three-phase evolution is usually found. The first phase is the ignition of the decane/air mixture at low values of η_1 . The second phase consists of the diffusion of species and energy from the autoignition spot, raising the temperature in mixture fracture space and additionally transferring species to higher values of η_1 and η_2 , hence igniting all mixture fractions. The third phase, if observed,

corresponds to the ignition of the line $\eta_1 = 0$, which represents the ammonia/air mixing line (zero decane). A description of these three phases follows.

The evolution of the solution starts with the ignition of the decane and low η_2 values as seen in Figure 8. The mixture is igniting at non-zero η_2 values which implies that a very lean, in

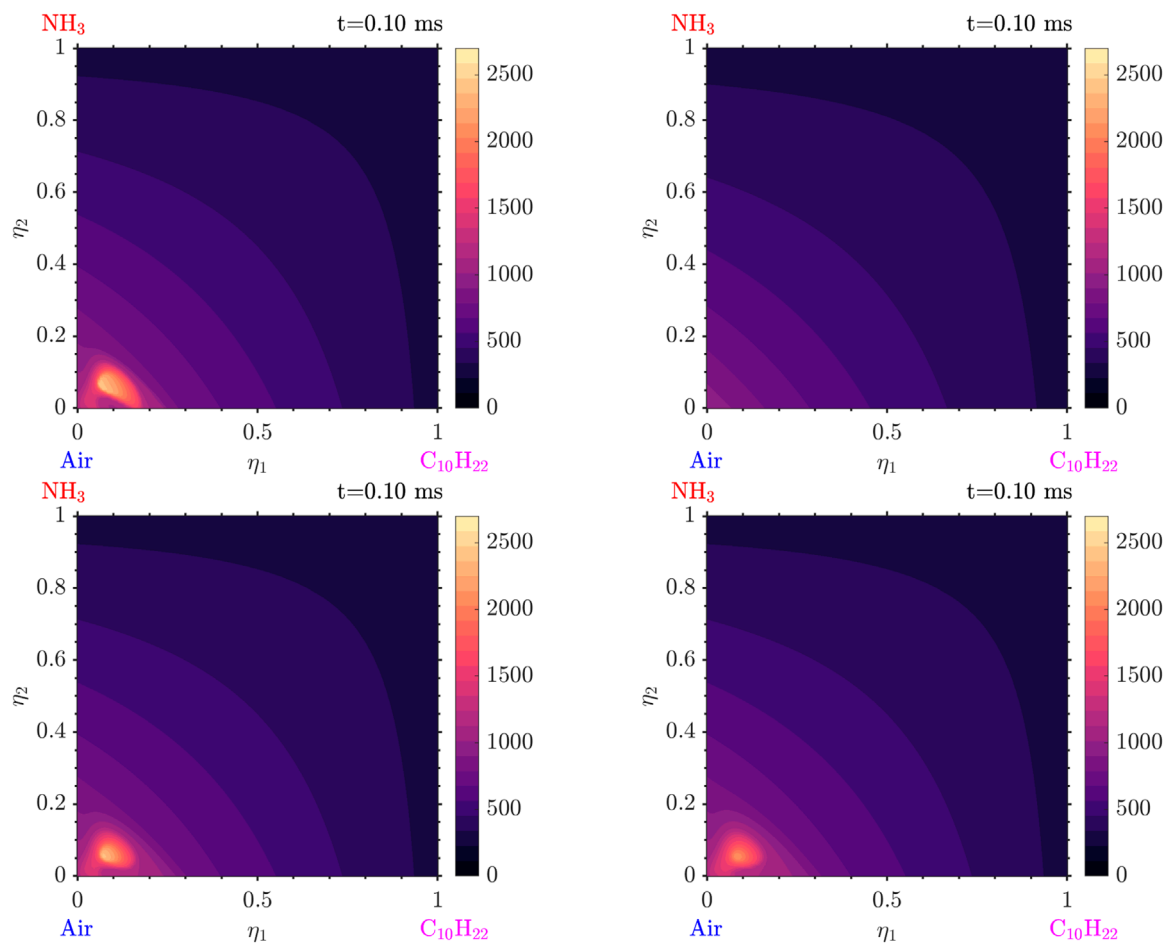


FIGURE 21

Distributions in $\eta_1 - \eta_2$ space of the temperature at $t = 0.1$ ms. From top left going clockwise: (A) $N_{\xi_1}, N_{\xi_2} = 1 \text{ s}^{-1}$ and $N_{\xi_1, \xi_2} = -0.5 \text{ s}^{-1}$; (B) $N_{\xi_1}, N_{\xi_2} = 10 \text{ s}^{-1}$ and $N_{\xi_1, \xi_2} = 5 \text{ s}^{-1}$; (C) $N_{\xi_1}, N_{\xi_2} = 50 \text{ s}^{-1}$ and $N_{\xi_1, \xi_2} = -25 \text{ s}^{-1}$; (D) $N_{\xi_1}, N_{\xi_2} = 25 \text{ s}^{-1}$ and $N_{\xi_1, \xi_2} = -12.5 \text{ s}^{-1}$.

terms of ammonia, decane-ammonia-air mixture is more reactive than a pure decane-air mixture. The ignition η_2 is lower than the most reactive mixture fraction of ammonia for the given conditions, and the ignition η_1 is slightly richer than the decane ξ_{mr} as quantified from the decane-air mixing layer analysis (Figure 7 for example).

Following that, very quickly, the $\eta_2 = 0$ line also ignites. The scale on the right is obtained from the maximum temperature reached after having analyzed the whole simulation. The ignition fronts rapidly evolve and move to the vicinity of ξ_{st} eventually reaching high temperatures for the whole region of mixture fractions smaller than 0.2 as seen in Figure 9. Figures 10, 11 shows the high CH_2O region migrating towards high values of η_1 and η_2 following the autoignition. Examining the same species along a single value of η_2 in Figure 12, we observe again the traverse as well as a single front traveling to the higher η_1 and a small one traveling to the low η_1 . Furthermore, from the two-dimensional distribution the diffusion and production of CH_2O in larger η_2 values is evident. The presence of combustion intermediates like CH_2O in a large range of mixture fractions suggests that in pilot-ignited diesel-ammonia systems we must consider the full mixture fraction evolutions and pollutant

generation and that the chemical scheme must be validated for very rich mixtures as well as lean ones.

Tracking the temperature as well as the mass fraction for the values of η_1 and η_2 corresponding to most the reactive mixture fraction respectively in Figure 13 the rapid increase of temperature is observed reaching around 2580 K after 0.6 ms. Additionally, the pre-ignition species OH is rapidly produced and destroyed. As seen from Figure 14 that shows the distribution along the decane-air line, decane is rapidly consumed, as seen by the curvature of the green line, producing also other intermediate species such as CO and H_2 at low η_1 . Once again, two fronts are seen for most species traveling across η_1 . The HO_2 forms three peaks, whereas OH forms two, one around the stoichiometry of the decane and one traveling to the right, indicating two reaction fronts.

Various species due to the presence of ammonia are also observed. In Figure 15 it is seen that the N_2O is generated around the ignition point but is eventually mainly produced in higher values of η_2 where the concentration of ammonia is greater (Figure 16). The initial front of N_2O has an interesting shape in the $\eta_1 - \eta_2$ distribution. The front becomes significantly thicker although the peak N_2O is reduced as it moves to larger η_2 diffusing at the same

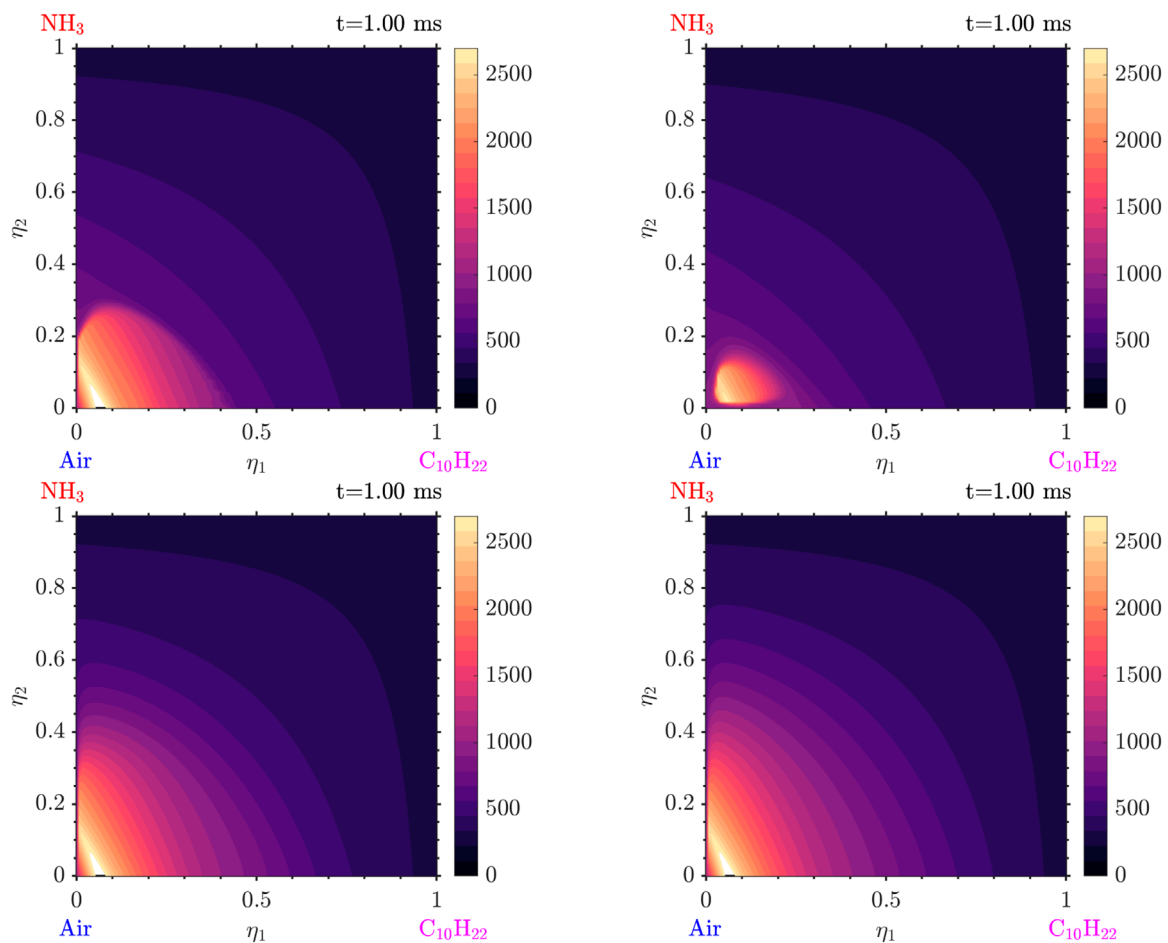


FIGURE 22

Distributions in $\eta_1 - \eta_2$ space of the temperature at $t = 1.00$ ms. From top left going clockwise: (A) $N_{\xi_1}, N_{\xi_2} = 1 \text{ s}^{-1}$ and $N_{\xi_1\xi_2} = -0.5 \text{ s}^{-1}$; (B) $N_{\xi_1}, N_{\xi_2} = 10 \text{ s}^{-1}$ and $N_{\xi_1\xi_2} = 5 \text{ s}^{-1}$; (C) $N_{\xi_1}, N_{\xi_2} = 50 \text{ s}^{-1}$ and $N_{\xi_1\xi_2} = -25 \text{ s}^{-1}$; (D) $N_{\xi_1}, N_{\xi_2} = 25 \text{ s}^{-1}$ and $N_{\xi_1\xi_2} = -12.5 \text{ s}^{-1}$.

time towards the $\eta_2 = 0$ line the same way the CH_2O is diffusing towards line $\eta_1 = 0$. The NH_3 consumption is more clear in Figure 17 where ammonia (the black line) is starting to be consumed (the curve assumes a curvature) while intermediate species such as NO and NO_2 are produced. In this figure, different species take very different shapes. The NO forms a double front while the CH_2O has one wide peak as seen before.

3.2.2 Intermediate phase

After autoignition, the flame grows across both mixture fractions. The diffusion flame of decane-air with no NH_3 ($\eta_2 = 0$) is eventually fully ignited and there are mixed flame structures for $\eta_2 > 0$ with progressively more presence of NH_3 . Figure 18 shows the η_2 distributions (i.e., along the ammonia-air line) of various species at a long time after ignition and for $\eta_1 = 0.097$, i.e., slightly richer than stoichiometry for decane. The consumption of NH_3 becomes clear, while the generation of CH_2O due to the consumption of decane is also evident. Hydrogen is growing due to the decomposition of ammonia and the pyrolysis of decane. OH is peaks at the decane-air flame (i.e., somewhere at the line $\eta_2 = 0$) and is consumed at higher values of η_2 .

3.2.3 Ignition of line $\eta_1 = 0$

The line $\eta_1 = 0$ corresponds to the air ammonia mixing line. Due to the Amplitude Mapping Model that gives $N_{\xi_1} = 0$ at $\eta_1 = 0$, no species reach this line from higher mixture fractions. As a result, due to the modelling choice of the scalar dissipation model (which is the usual model in both flamelet and CMC models), this boundary follows its own characteristic time evolution. There are again pre-ignition species such as HO_2 that are rapidly produced and consumed as well as some products such as H_2 (not shown). We also see that N_2O is produced during the consumption of ammonia, which is depicted in Figure 19 where a single front forms. This front again travels to larger η_2 values and peaks around the stoichiometry of ammonia. The same is true for the temperature distribution in Figure 20. Initially, as seen even after 1 ms the distribution is exactly the same as the initial conditions. At some point, the line starts igniting eventually forming a front that is heading to larger η_2 . The maximum temperature is smaller, as expected from pure ammonia, in this region. The distribution at the latest time shown in Figure 20 is similar to a conventional non-premixed autoigniting system at the moment of autoignition (Mastorakos, 2009).

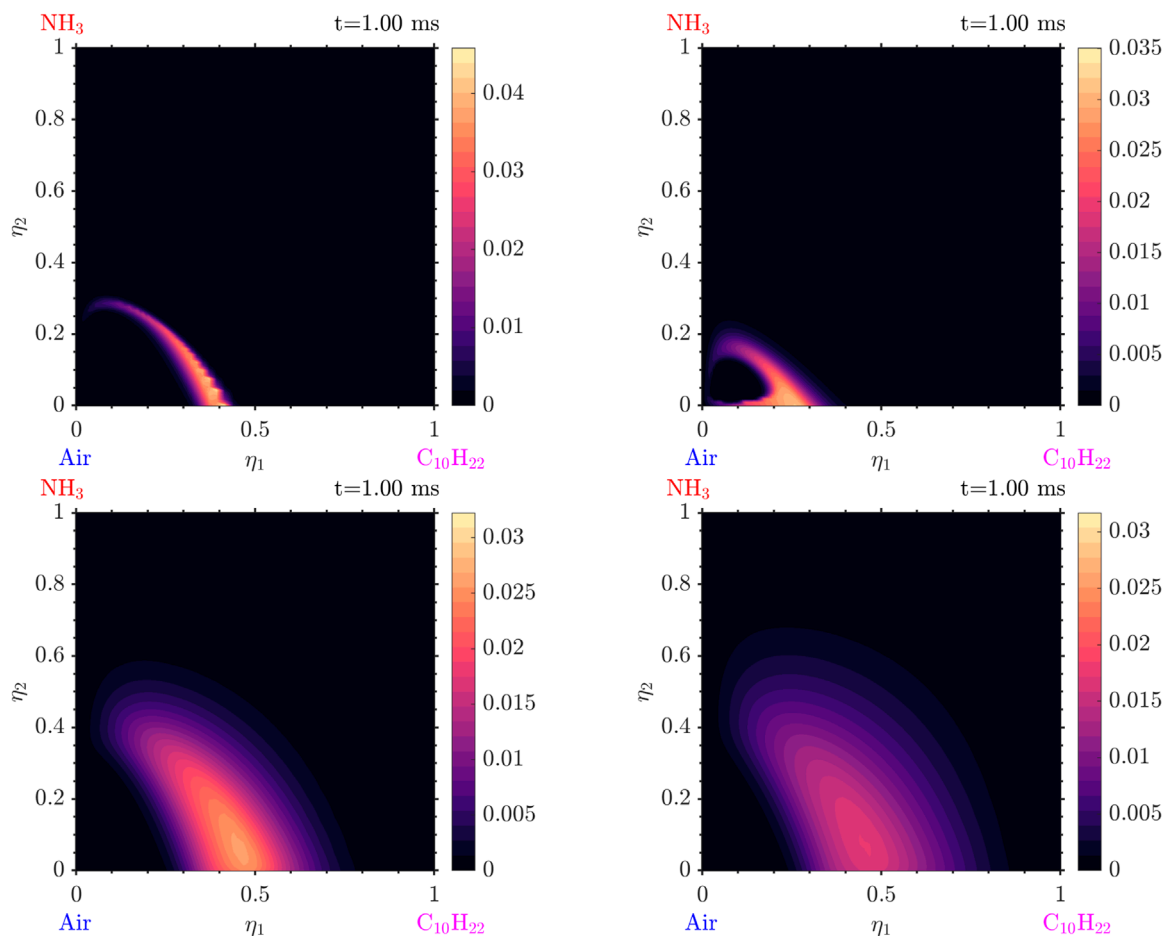


FIGURE 23

Distributions in $\eta_1 - \eta_2$ space of the CH_2O at $t = 1.0$ ms. From top left going clockwise: (A) $N_{\xi_1}, N_{\xi_2} = 1 \text{ s}^{-1}$ and $N_{\xi_1\xi_2} = -0.5 \text{ s}^{-1}$; (B) $N_{\xi_1}, N_{\xi_2} = 10 \text{ s}^{-1}$ and $N_{\xi_1\xi_2} = 5 \text{ s}^{-1}$; (C) $N_{\xi_1}, N_{\xi_2} = 50 \text{ s}^{-1}$ and $N_{\xi_1\xi_2} = -25 \text{ s}^{-1}$; (D) $N_{\xi_1}, N_{\xi_2} = 25 \text{ s}^{-1}$ and $N_{\xi_1\xi_2} = -12.5 \text{ s}^{-1}$.

3.2.4 Effects of scalar dissipation rates

Simulations with various values of scalar dissipation were performed. Examining Figures 21, 22 we observe that a positive cross-scalar dissipation rate leads to later ignition in comparison to a negative cross scalar dissipation rate. Additionally, we observe that for a higher magnitude of scalar dissipation rate the ignition is delayed in comparison to the smaller ones. Moreover, the difference in ignition time when the scalar dissipation rate is small is insignificant, as suggested by Mastorakos (2009) from analysis of autoignition in single mixture fraction. As the scalar dissipation increases, eventually autoignition does not occur, as expected (not shown here). Analyzing the evolution of the solution from Figure 23 it is evident that the diffusion of radicals is altered judging from the conditional mass fraction of CH_2O . The phenomenon again is slower for the positive cross-scalar dissipation rate. It is interesting that for high scalar dissipation rates N_{ξ_1} and N_{ξ_2} the diffusion of the radicals is faster to higher η_1 but with lower magnitude. The small scalar dissipation rate produces a thinner front with a higher concentration.

Other findings include the following: as the scalar dissipation rate increases slightly smaller temperatures and slightly reduced

amounts of radicals are observed. An interesting point is that, due to the different scalar dissipation rates, each mixture ignites in a different η_1 and η_2 . This suggests that each fuel might be behaving differently concerning the scalar dissipation rates as each fuel has its own critical scalar dissipation rate (the scalar dissipation rate over which ignition does not take place due to the very strong mixing). As the decane is already very reactive, this leads to very high critical scalar dissipation rates for the decane-ammonia mixture. However, high values of scalar and cross-scalar dissipation rates do not allow the ammonia-air line to ignite. Also, it is observed that the production of some radicals and pollutants is changing.

In general, it is observed that high values of scalar dissipation rates can slow down reactions and therefore delay autoignition in those areas. On the contrary, the low scalar dissipation rates allow for the accumulation of species with time and temperature for the reactions to occur faster and more strongly. As a result in the general case of a flow, the mixture is expected to firstly ignite in the regions with low scalar dissipation rates and less intense mixing.

It is evident that for use in a turbulent reacting flow simulation, the magnitude of the two scalar dissipation rates, but also of the cross scalar dissipation rate, can make a large difference to the autoignition

time and the evolution of species, and hence pollutants, as a function of time. Further research is needed in this area.

4 Conclusion

Simulations in a two-dimensional mixture fraction space with prescribed scalar dissipation and cross scalar dissipation rates were performed to provide insights to non-premixed autoignition of a decane-ammonia-air system. Such situations may be expected in novel ammonia engines with direct injection of both fuels and the present results offer some basic understanding of the underlying canonical problems. Due to its higher reactivity, decane ignites first and then this creates reaction fronts that move across both mixture fractions to establish eventually the non-premixed flames. For low values of the scalar dissipation, its value does not affect the autoignition time significantly, however for large values autoignition is delayed. The cross-scalar dissipation (sign and magnitude) can make a large difference in the evolution of the system, as it affects the diffusion of heat and species from the autoignition spot to the remaining unburnt fluid. Positive cross scalar dissipation leads to later autoignition compared to negative values, suggesting a diffusion of radicals into the ammonia-air mixture that act as a sink, hence delaying thermal runaway.

The present results provide a first evaluation of Doubly-Conditioned Moment Closure for hydrocarbon-ammonia systems and the results suggest that care is needed with the modelling of the cross scalar dissipation rate.

Data availability statement

The raw data supporting the conclusions of this article will be made available by the authors, without undue reservation.

Author contributions

AK: Data curation, Formal Analysis, Investigation, Methodology, Writing—original draft. EM: Conceptualization,

References

- Alan, C. H. (1983). *Odepack, a systemized collection of ode solvers*. Washington, Scientific computing.
- Bilger, R. W. (1993). Conditional moment closure for turbulent reacting flow. *Phys. Fluids A Fluid Dyn.* 5 (2), 436–444. doi:10.1063/1.858867
- Chakraborty, N., Mastorakos, E., and Cant, R. S. (2007). Effects of turbulence on spark ignition in inhomogeneous mixtures: a direct numerical simulation (dns) study. *Combust. Sci. Technol.* 179 (1–2), 293–317. doi:10.1080/00102200600809555
- Chin, L. L., Foscoli, B., Mastorakos, E., and Evans, S. (2021). A comparison of alternative fuels for shipping in terms of lifecycle energy and cost. *Energies* 14 (24), 8502. doi:10.3390/en14248502
- Curran, S., Onorati, A., Payri, R., Kumar Agarwal, A., Arcoumanis, C., Bae, C., et al. (2024). The future of ship engines: renewable fuels and enabling technologies for decarbonization. *Int. J. Engine Res.* 25 (1), 85–110. doi:10.1177/14680874231187954
- Harikrishnan, B., Gkantonas, S., and Mastorakos, E. (2024). *LES-DCMC of dual-fuel ignition problems*. American Institute of Aeronautics and Astronautics. doi:10.17863/CAM.104482
- International Maritime Organization (2015). *Third IMO GHG study 2014*. London: International Maritime Organization.
- Joung, T.-H., Kang, S.-G., Lee, J.-K., and Ahn, J. (2020). The imo initial strategy for reducing greenhouse gas (ghg) emissions, and its follow-up actions towards 2050. *J. Int. Marit. Saf. Environ. Aff. Shipp.* 4 (1), 1–7. doi:10.1080/25725084.2019.1707938
- Klimenko, A. Y., and Bilger, R. W. (1999). Conditional moment closure for turbulent combustion. *Prog. Energy Combust. Sci.* 25 (6), 595–687. doi:10.1016/s0360-1285(99)00006-4
- Kronenburg, A. (2004). Double conditioning of reactive scalar transport equations in turbulent nonpremixed flames. *Phys. Fluids* 16 (7), 2640–2648. doi:10.1063/1.1758219
- Lin Tay, K., Yang, W., Li, J., Zhou, D., Yu, W., Zhao, F., et al. (2017). Numerical investigation on the combustion and emissions of a kerosene-diesel fueled compression ignition engine assisted by ammonia fumigation. *Appl. Energy* 204, 1476–1488. doi:10.1016/j.apenergy.2017.03.100
- MAN Energy Solutions (2023). *Man bw two-stroke engine operating on ammonia*. Available at: <https://www.man-es.com/docs/default-source/marine/tools/man-bw-two-stroke-engine-operating-on-ammonia.pdf>, (Accessed August 21, 2024).

Funding acquisition, Investigation, Project administration, Resources, Supervision, Writing—review and editing.

Funding

The author(s) declare that financial support was received for the research, authorship, and/or publication of this article. This research was partly funded by the National Research Foundation (NRF), Prime Minister's Office, Singapore, under its Campus for Research Excellence and Technological Enterprise (CREATE) programme.

Acknowledgments

We wish to thank Drs. S. Gkantonas and B. Hariskrishnan for their help with the code. This research was partly funded by the National Research Foundation (NRF), Prime Minister's Office, Singapore, under its Campus for Research Excellence and Technological Enterprise (CREATE) programme. For the purpose of open access, the authors have applied a Creative Commons Attribution (CC BY) license to any Author Accepted Manuscript version arising from this submission.

Conflict of interest

The authors declare that the research was conducted in the absence of any commercial or financial relationships that could be construed as a potential conflict of interest.

Publisher's note

All claims expressed in this article are solely those of the authors and do not necessarily represent those of their affiliated organizations, or those of the publisher, the editors and the reviewers. Any product that may be evaluated in this article, or claim that may be made by its manufacturer, is not guaranteed or endorsed by the publisher.

- Mastorakos, E. (2009). Ignition of turbulent non-premixed flames. *Prog. Energy Combust. Sci.* 35 (1), 57–97. doi:10.1016/j.pecs.2008.07.002
- O'Brien, E. E., and Jiang, T.-L. (1991). The conditional dissipation rate of an initially binary scalar in homogeneous turbulence. *Phys. Fluids A Fluid Dyn.* 3 (12), 3121–3123. doi:10.1063/1.858127
- Perini, F., Galligani, E., and Reitz, R. D. (2012). An analytical jacobian approach to sparse reaction kinetics for computationally efficient combustion modeling with large reaction mechanisms. *Energy and Fuels* 26 (8), 4804–4822. doi:10.1021/ef300747n
- Perry, B. A., Mueller, M. E., and Masri, A. R. (2017). A two mixture fraction flamelet model for large eddy simulation of turbulent flames with inhomogeneous inlets. *Proc. Combust. Inst.* 36 (2), 1767–1775. doi:10.1016/j.proci.2016.07.029
- Peters, N. (2001). Turbulent combustion. *Meas. Sci. Technol.* 12 (11), 2022. doi:10.1088/0957-0233/12/11/708
- Philip, S. M. (2019). Modelling of spray combustion with doubly conditional moment closure. *Flow, Turbulence and Combustion.* 96, 933.
- Philip Sitte, M., and Mastorakos, E. (2019). Large eddy simulation of a spray jet flame using doubly conditional moment closure. *Combust. flame* 199, 309–323. doi:10.1016/j.combustflame.2018.08.026
- Poinsot, T., and Veynante, D. (2005). *Theoretical and numerical combustion*. Philadelphia: RT Edwards Inc.
- Ramanathan, A., Dharmalingam, B., and Thangarasu, V. (2023). *Advances in clean energy*. Boca Raton: CRC Press. 1. doi:10.1201/9781003055686
- Simon, B., Mason, J., Broderick, J., and Larkin, A. (2020). Shipping and the paris climate agreement: a focus on committed emissions. *BMC Energy* 2 (1), 5. doi:10.1186/s42500-020-00015-2
- Thorsen, L. S., Jensen, M. S. T., Pullich, M. S., Christensen, J. M., Hashemi, H., Glarborg, P., et al. (2023). High pressure oxidation of nh₃/n-heptane mixtures. *Combust. Flame* 254, 112785. doi:10.1016/j.combustflame.2023.112785
- Tolga Kurumus, A., Bhattacharya, A., Tamadonfar, P., and Kaario, O. (2024). A skeletal mechanism for n-dodecane/ammonia combustion and an open-source reaction scheme optimization tool. *Fuel* 373, 132168. doi:10.1016/j.fuel.2024.132168
- United Nations (2018). Review of Maritime transport 2018, in United Nations Conference on Trade and Development (UNCTAD), Geneva, 30 December 1964.
- UNFCCC (2024). United Nations Framework Convention on Climate Change (UNFCCC). *The paris agreement*. Available at: https://en.wikipedia.org/wiki/United_Nations_Framework_Convention_on_Climate_Change (Accessed: 2024-January-23).
- Valera-Medina, A., Xiao, H., Owen-Jones, M., David, W. I. F., and Bowen, P. J. (2018). Ammonia for power. *Prog. Energy Combust. Sci.* 69, 63–102. doi:10.1016/j.pecs.2018.07.001
- Wong, A. Y. H., Selin, N. E., Eastham, S. D., Mounaïm-Rousselle, C., Zhang, Y., and Allroggen, F. (2024). Climate and air quality impact of using ammonia as an alternative shipping fuel. *Environ. Res. Lett.* 19, 084002. doi:10.1088/1748-9326/ad5d07
- Yu, P., and Watanabe, H. (2023). A simplified two-mixture-fraction-based flamelet modelling and its validation on a non-premixed staged combustion system. *Combust. Theory Model.* 27 (1), 37–56. doi:10.1080/13647830.2022.2144460
- Zhou, X., Li, T., Chen, R., Wei, Y., Wang, X., Wang, N., et al. (2024). Ammonia marine engine design for enhanced efficiency and reduced greenhouse gas emissions. *Nat. Commun.* 15 (1), 2110. doi:10.1038/s41467-024-46452-z